Progress In Electromagnetics Research C, Vol. 160, 143–153, 2025

PIER C

(Received 1 January 2025, Accepted 26 August 2025, Scheduled 28 September 2025)

Magnetostrictive Vibration Behavior of an Amorphous Alloy Transformer Featuring a Three-Dimensional Coil Core

Romaric K. Noubissi[1], Daosheng Liu[1,*], and Boxue Du[2]

[1]*School of Electrical Engineering and Automation, Jiangxi University of Science and Technology, Ganzhou 341000, China*
[2]*School of Electrical Engineering and Information, Tianjin University, Tianjin 300072, China*

ABSTRACT: The novel amorphous alloy transformer featuring a closed three-dimensional coil core (CTDCC) represents an innovative approach to transformer structure. In contrast to the conventional three-phase five-column transformer equipped with a planar coil core (PCC), the CTDCC configuration displays a completely equal magnetic circuit, leading to improved short-circuit tolerance. Nevertheless, the design and manufacturing process of the core faces a notable engineering obstacle due to the amplified magnetostrictive coefficient of the amorphous alloy, resulting in vibration noise. In order to address this issue, a magnetic-mechanical coupling mathematical model is developed in this research to analyze the magnetostrictive effect of the amorphous alloy CTDCC. Three-dimensional finite element analysis (FEA) is utilized to compute the magnetic flux distribution and quivering dislocation dissipation of the CTDCC. Furthermore, a validation experiment is carried out on a 30 kVA amorphous alloy CTDCC model to confirm the precision of the model. Moreover, the CTDCC structure has been proven to effectively minimize surface vibrations compared to the PCC model. Additionally, it unveils the governing frequency law of vibration movement at various locations within the CTDCC structure. This revelation serves as a fundamental basis for developing strategies to mitigate vibrations and control noise during the CTDCC design.

1. INTRODUCTION

Amorphous alloy constituents exhibit remarkable characteristics of high permeability and low loss, leading to a substantial reduction in the no-load loss of transformers. This reduction in loss contributes to achieving energy efficiency, as demonstrated in [1, 2]. The magnetostrictive properties of amorphous alloy material are notably greater than silicon steel, resulting in heightened levels of vibration and noise, as evidenced by [3–5]. Planar coil core (PCC) and closed three-dimensional coil core (CTDCC) stand out as the predominant core design utilized in amorphous alloy transformers, with their respective features outlined in Table 1. Vibration characteristics of CTDCC are significantly distinct from those of PCC due to structural variances. In contrast to PCC, CTDCC offers benefits such as robust resistance to abrupt short circuits, compact dimensions, and cost-effectiveness.

Previously, numerous studies have been conducted on amorphous transformer cores, with primary emphasis on three key areas: core magnetic properties, magnetostrictive force, and core vibration features. The core magnetic properties were analyzed by investigating features of the magnetic flux density dissipation within PCC and CTDCC under diverse excitation states, as demonstrated in [6, 7]. The impact of magnetic permeability on magnetostrictive force, the force exerted on the core in electromagnetic field, and the alteration of inner stress due to magnetostriction were investigated using the technique of imaginary movement, as demonstrated in [8, 9]. The magneto-mechanical feeble coupling problematic is analyzed using finite element analysis (FEA), taking into account magnetostriction. The calculation of magnetostrictive force is performed using elastic mechanics technique, as illustrated in [10–12]. Studies conducted by [13, 14] have examined simulations of transformer cores, revealing that the primary factor responsible for the transformer core vibration is the magnetostrictive strength, as opposed to the electromagnetic force. The vibration properties of single-phase amorphous alloy planar coil cores have been investigated considering different support boundary settings [15]. A vibration experiment stage is constructed to perform a comparative analysis of vibration dislocation features for single-frame cores, two-frame single-phase transformers, and three-frame three-phase transformers [16]. The magnetic flux of the three-dimensional wound core transformer was established in [17] through the application of H-balance equation. Increasing the mass at the maximum vibration position of the transformer box optimized the natural frequency and modal amplitude of the transformer structure [18].

In conclusion, planar coil core amorphous transformers are frequently employed by researchers to investigate and compute vibrations resulting from magnetostriction. However, with the progress in manufacturing techniques, users are now showing a growing interest in transformers featuring innovative core structures like CTDCC. Nevertheless, there exists a dearth of research on the vibration and sound analysis pertaining to these innovative core assemblies, such as CTDCC. The dissimilarities in vibration movement features between CTDCC and PCC have yet to be elucidated. The investigation of vibration properties of amorphous alloy transformers utilizing CTDCC demon-

---

* Corresponding author: Daosheng Liu (daoshengliu@aliyun.com).

doi:10.2528/PIERC25010102

Published by THE ELECTROMAGNETIC ACADEMY

TABLE 1. CTDCC and PCC differentiation.

Core Type	PCC	CTDCC
Structure assemblage	Four individual cores positioned linearly	Three single cores configured triangularly
Cross-section	Quadrilateral	Almost Rotund
Magnetic circuit lengths per phase	Unequal	Identical

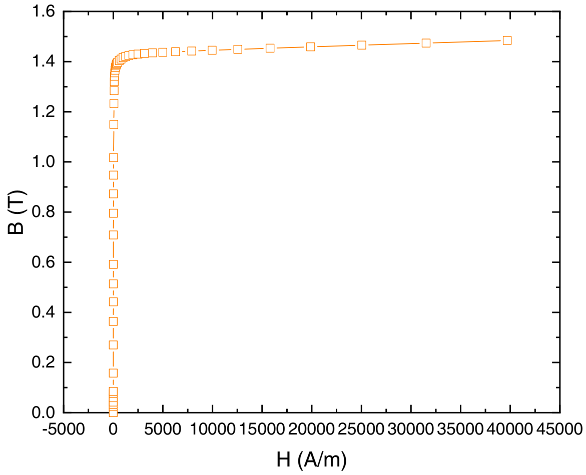

FIGURE 1. Magnetization graph of amorphous core.

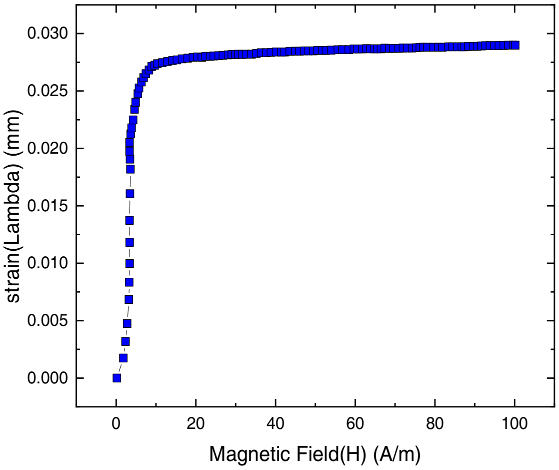

FIGURE 2. Relationship between the magnetostriction and magnetic flux density.

strates notable significance in both engineering and academic fields.

The main contribution of this paper is to minimize the surface vibration displacement transformer core by using a new structural design (CTDCC) through the finite element analysis and experimental platform and comparing CTDCC with PCC. CTDCC has a significant level of mechanization that primarily pertains to the formation of cores, which is produced using a core winding machine. In contrast to the conventional stacked core, this method exhibits a higher degree of mechanization, presenting a substantial advantage in the mass production of distribution transformers. Uniformity of the distribution of the magnetic circuit, a three-phase magnetic circuit, exhibits perfect symmetry, accompanied by a total equilibrium of the no-load current [19].

In order to tackle the aforementioned concerns, this research delves into the analysis of two kinds of amorphous transformers equipped with a CTDCC and a PCC, each boasting a 30 kVA capacity. The key findings of this study are outlined as follows:

1) Finite Element Analysis (FEA) is utilized for the calculation and comparison of the vibration displacement for the core surface.

2) The experimental setup has been completed, with the positions carefully organized in conjunction with the core design. The study investigates the vibration displacement dissipation for two different core types, thereby confirming the simulation precision.

3) A study on the vibration properties of the CTDCC under various operational circumstances has been carried out, offering a theoretical basis for the development of strategies to reduce vibration and control noise in amorphous transformers.

2. SYSTEMATIC APPROACH

2.1. Properties of Magnetization and Magnetostriction

Obtaining precise magnetic property graph is crucial for determining the parameters needed to analyze the magnetic and vibration properties of amorphous transformer cores under normal operation [20]. The B-H curve of the amorphous alloy core is depicted in Fig. 1.

Magnetostriction, an intrinsic characteristic of magnetic materials, causes a change in the size of amorphous alloy materials along the magnetic induction direction when being subjected to an alternating magnetic field. This phenomenon, known as magnetostriction, leads to slight deformations [3].

Consequently, the amorphous alloy transformer core undergoes periodic vibrations at twice the excitation frequency. Fig. 2 illustrates the magnetostriction-flux density relationship for the amorphous alloy strip. The magnetostrictive peak-to-peak value, denoted as λ_{pp}, is ascertained by employing Eq. (1) for various flux densities.

$$\lambda_{pp} = \lambda_{\max} - \lambda_{\min} \tag{1}$$

The values $\lambda_{\max}$ and $\lambda_{\min}$ represent the utmost expansion and contraction, respectively, experienced by ferromagnetic materials due to the phenomenon of magnetostriction.

By analyzing the magnetostrictive peak-to-peak value flux density curve, it is possible to determine the extent of deformation resulting from the magnetostriction of the transformer core at various flux densities. This information enables the calculation of stress and vibration acceleration experienced by the cores.

2.2. Theoretic Analysis Coupling

2.2.1. Magnetic Field

The main focus of this study is to analyze the vibration properties of the amorphous transformer cores at power frequency. As a result, the magnetic field within the core is considered to be a magnetic quasi-static field, and the shift current is ignored, and Maxwell's equations can be formulated accordingly [3].

$$\nabla \times \mathbf{H} = \mathbf{J} \tag{2}$$

$$\nabla \times \mathbf{E} = \frac{\partial \mathbf{B}}{\partial t} \tag{3}$$

In this context, **H** represents the magnitude of the magnetic field (A/m); **J** denotes the density of the conduction current (A/m^2); **E** signifies the intensity of the electric field (V/m); **B** represents the density of the flux (T); and t denotes the variable of time (s).

In order to streamline the computation process, the vector magnetic potential **A** is utilized, where **B** is defined as ∇***A**. By introducing Eq. (2), the differential equation for the vector magnetic potential in the core can be derived.

$$\nabla \times (v\nabla \times \mathbf{A}) = \mathbf{J} \tag{4}$$

The magnetoresistance rate, denoted as **v**, is defined by equation $\mathbf{H} = \mathbf{vB}$, where **H** is the magnetic field strength and B the magnetic induction. The value of **v** is determined to be identical to the reciprocal of the permeability, $\mathbf{v} = 1/\boldsymbol{\mu}$.

2.2.2. Stress

In this investigation, the magnetostrictive equivalent stress of the core is determined by incorporating the amorphous core, disregarding the interaction among the layers of the amorphous strip. The relationship between magnetostrictive strain and magnetostrictive stress can be determined by applying the stress-strain rapport of elastic mechanics, as demonstrated in [21–23]. Subsequently, the body load is computed and examined. The matrix representation of stress-strain correlation in three dimensions is presented below.

$$\boldsymbol{\sigma} \times D\boldsymbol{\varepsilon} \tag{5}$$

The stress vector is denoted by $\boldsymbol{\sigma}$, while the strain vector is represented by ε. The elastic matrix, D, can be expressed as follows.

$$D = \frac{E(1-\alpha)}{(1+\alpha)(1-2\alpha)} \begin{pmatrix} 1 & \frac{a}{1-\alpha} & \frac{a}{1-\alpha} & 0 & 0 & 0 \\ \frac{a}{1-\alpha} & 1 & \frac{a}{1-\alpha} & 0 & 0 & 0 \\ \frac{a}{1-\alpha} & \frac{a}{1-\alpha} & 1 & 0 & 0 & 0 \\ 0 & 0 & 0 & \frac{1-2\alpha}{2(1-\alpha)} & 0 & 0 \\ 0 & 0 & 0 & 0 & \frac{1-2\alpha}{2(1-\alpha)} & 0 \\ 0 & 0 & 0 & 0 & 0 & \frac{1-2\alpha}{2(1-\alpha)} \end{pmatrix} \tag{6}$$

The material's Poisson's ratio, denoted by $\boldsymbol{\alpha}$, and Young's modulus, denoted by **E**, are two important parameters in the field of materials science.

The magnetostrictive stress of the three-dimensional wound core is determined using Eqs. (5) and (6), leading to the calculation of the magnetostrictive volume force upon the introduction of Eq. (7).

$$\nabla \cdot \boldsymbol{\sigma} = -\mathbf{F}_v \tag{7}$$

The magnetostrictive body force is denoted as $\mathbf{F}_v$.

2.2.3. Displacement

Disregarding the damping effect caused by the core, the differential equation governing structural force field can be expressed as follows.

$$\mathbf{M}\frac{d^2\mathbf{u}}{dt^2} + \mathbf{Ku} = \mathbf{F}_V \tag{8}$$

The mass matrix is denoted by **M**, stiffness matrix denoted by **K**, and dislocation vector denoted by **u**.

Through the solution of Eq. (8), it is possible to determine the vibration shift vector of the core, leading to the acquisition of core overall vibration characteristics.

3. COMPUTATION OF PCC AND CTDCC

3.1. Design of the Model

In order to validate the precision of the recorded magnetic properties data for the amorphous alloy and enhance the analysis and prediction of the amorphous alloy transformer core vibration, a three-dimensional Finite Element Analysis (FEA) model is constructed for amorphous alloy Planar Coil Core (PCC) and Closed Three-Dimensional Coil Core (CTDCC). The locations for extracting vibration displacement on each core surface during computation are denoted as locations A, B, for PCC as shown in Fig. 3(a), and C, for CTDCC as illustrated in Fig. 3(b).

In order to analyze the vibration properties of amorphous alloys PCC and CTDCC, the magnetic flux density within the inner chamfer of the core is standardized at 1.407 T, followed by the individual calculation of the vibration displacement properties on the core surface. The characteristics of the amorphous alloy core are detailed in Table 2. The coil consists of copper and surrounded by air in proximity to the core.

TABLE 2. Computation constraints.

Parameters	Unit	Value	
		PCC	CTDCC
Cross-section	m^2	0.031	0.033
Number of turns for excitation	Turns	25	10
Magnetic flux density	T	1.4075	1.4078
Voltage	V	230.9	27.81
Young's modulus	GPa	110	110
Poisson ratio	-	0.3	0.3

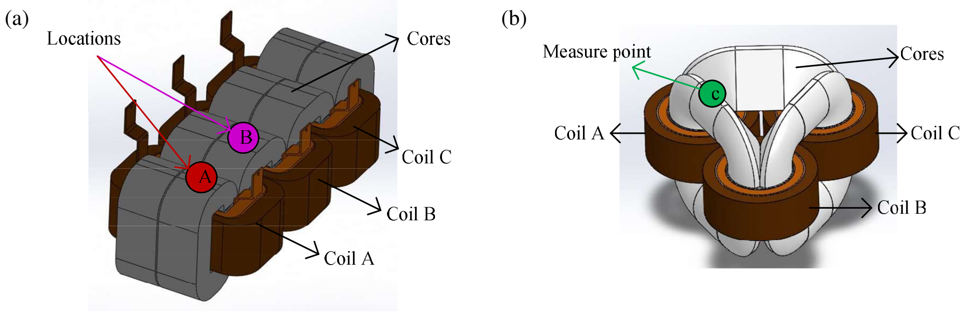

FIGURE 3. Design of the cores studied; (a) PCC structure, (b) CTDCC.

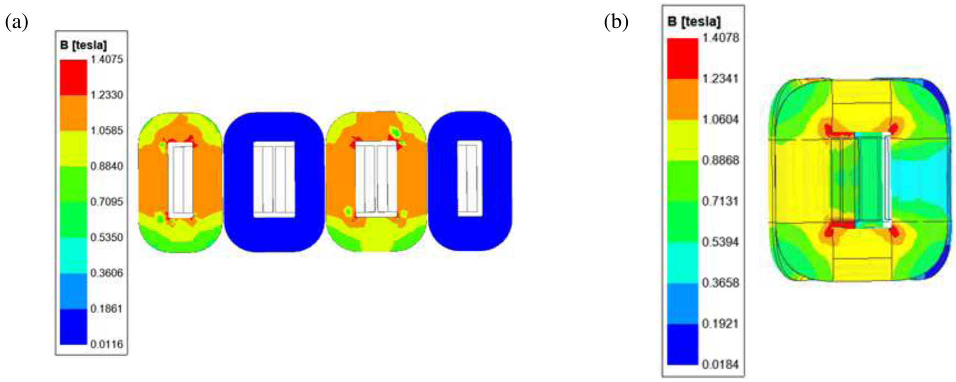

FIGURE 4. Flux density distribution; (a) PCC, (b) CTDCC.

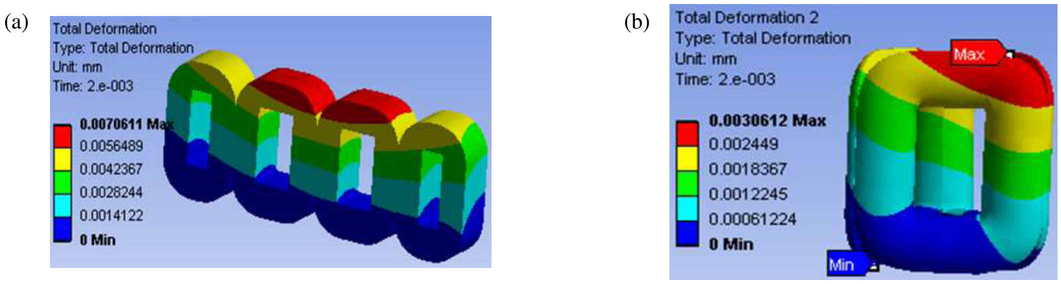

FIGURE 5. Vibratory magnitude dissipation; (a) PCC displacement, (b) CTDCC displacement.

3.2. PCC, CTDCC Magnetic Field and Displacement

Figures 4(a) and 4(b) illustrate the flux density dissipation computation graph of PCC and CTDCC structures respectively at 12 ms across the z-direction segment of the core frame. The data presented in the chart indicates that the density of both cores is higher in the inner chamfer of the core with an amplitude of 1.407 T, while it decreases towards the outer edges of the core. The dissipation of flux density on the top core surface is quite consistent, with an average flux density of 1.233 T and 1.06 T respectively in Figs. 4(a) and 4(b). It can be observed that the flux density distribution on the core column of the PCC is larger than the CTDCC. Hence, the CTDCC structure design minimizes the flux density on the core.

By utilizing the solid mechanics module within the ANSYS software and incorporating the magnetostrictive-magnetic flux density graph of the amorphous alloy as an input, the module is able to compute the distribution of surface displacement for the cores. Linear material parameters were applied in the simulation of magnetic fields, while careful consideration was given to the modeling of surrounding air. The analysis demonstrates that the displacement generated by a triangular core transformer exhibits a more rapid decay than those produced by a planar coil core transformer.

The vibratory shift of the two cores exhibits a gradual decrease from the top section to inferior section, as illustrated in Fig. 5. The top surface of the cores exhibits the highest average oscillation displacement, while the vibratory magnitudes of the core columns on the right and left are equal, being symmetrically dissipated on either side of the core frame. The peak displacement of the PCC and CTDCC is situated at the junction of the upper core and the core column, measuring 1.41×10^{-6} m, and 0.61×10^{-6} m correspondingly.

The comparison between the computation of the vibratory displacement on the top CTDCC and PCC surface is illustrated

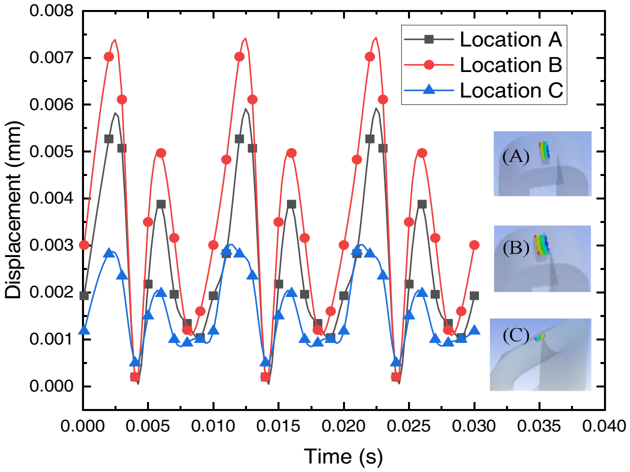

FIGURE 6. Comparison of vibratory displacement computation between the PCC and CTDCC.

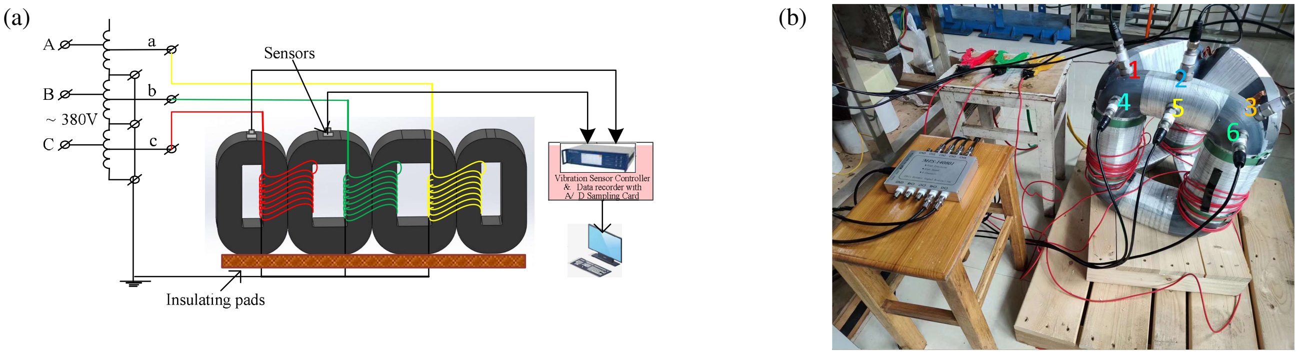

FIGURE 7. Experiment platform; (a) PCC testing, (b) CTDCC testing.

in Fig. 6. It can be deduced that at the same flux density, PCC exhibits a higher vibration displacement magnitude than CTDCC. Consequently, the vibration experienced by the PCC structure will be more serious, leading to an increase in noise levels. The CTDCC structure has the capability to reduce surface vibrations within the cores, thus partially alleviating the noise produced by the amorphous alloy transformer. The vibration displacement on the core column of the PCC is larger than the CTDCC with an average value of 3.5×10^{-6} m and 1.8×10^{-6} m, respectively. The maximal oscillation is represented at 2 ms, with values of 5.27×10^{-6} m, 7.02×10^{-6} m, and 2.82×10^{-6} m correspondingly to the studied locations A, B, and C, where locations A and B are for the PCC, and location C is for the CTDCC.

4. EXPERIMENTAL SETUPS

4.1. Testing Comparison of PCC and CTDCC

Additionally, to gain a deeper understanding of vibration properties exhibited by amorphous alloy transformer cores with diverse model and to validate the accuracy of the vibration displacement calculated through computation model, separate vibration experiments are conducted on the PCC and CTDCC. The experimental samples can be observed in Fig. 7. The amplitude of the three-phase AC supply matches the simulation values, with 230.9 V and 27.81 V correspondingly, while the frequency remains at 50 Hz. The quantity of excitation coils corresponds to the computation value, which is 25 turns and 10 turns.

A power supply with three phases is utilized to supply voltage at the power frequency to the core. Additionally, a power analyzer is employed to monitor and log the excitation signal applied, while a piezoelectric vibration acceleration sensor is utilized to gauge the surface vibration of the core and transfer the data to the computer.

Given that the acceleration sensor gauges the vibration along the thickness axis of the rectangular cross-section of the PCC, and the recorded measurement is smaller than that of the top surface. The impact on the overall core vibration magnitude is comparatively minimal. Hence, the positioning of measurements is limited to the top surface of the small and large core frames of PCC. This can be observed in Fig. 8(a). The CTDCC is characterized by a closely semi-circular cross-section on the top yoke, leading to a vibration that displays a superposition principle on the topmost yoke. Furthermore, the three core frames exhibit an assemblage that is totally symmetrical and shaped like an equilateral triangle. Hence, the location of vibration measurement points would be concentrated on a sin-

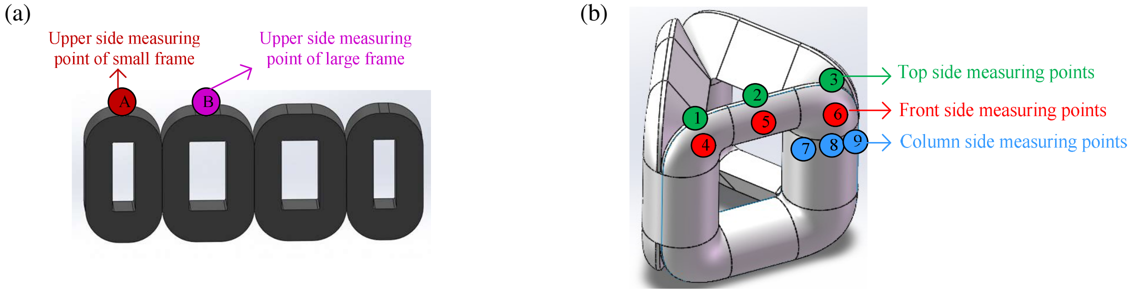

FIGURE 8. Measuring locations. (a) PCC, (b) CTDCC.

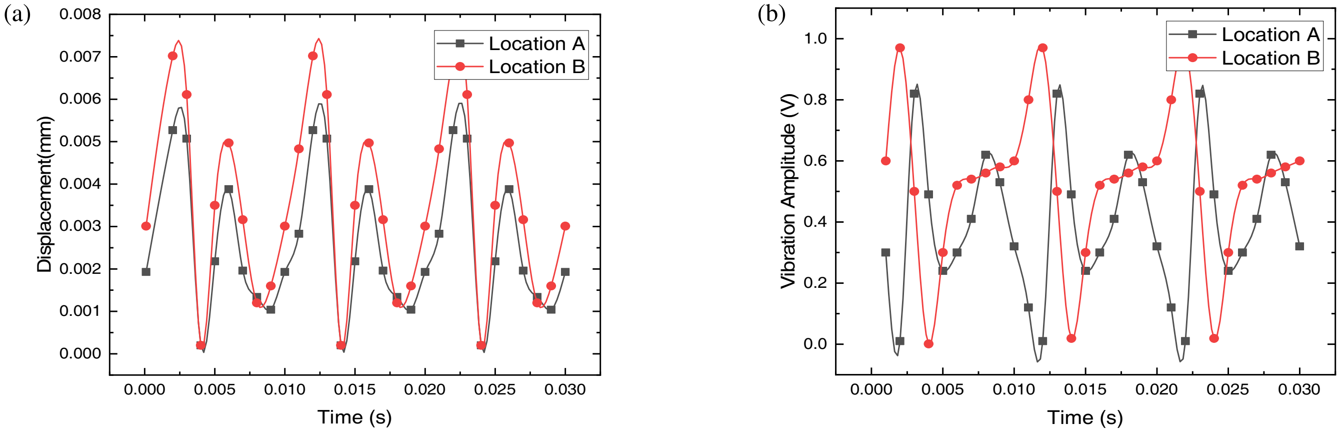

FIGURE 9. Evaluation of vibration displacement computation and testing of the PCC; (a) Simulation, (b) Testing.

gle core frame. The measuring locations on the upper surface range from 1 to 3; the front side surface ranges from 4 to 6; and the core column ranges from 7 to 9, as illustrated in Fig. 8(b).

5. RESULTS AND DISCUSSIONS

5.1. Evaluation of PCC and CTDCC

In Fig. 9, a comparison between the simulated vibration displacement and the experiment of measurement position of the PCC reveals that the vibration displacement of the large core frame (Position B) is higher than that of the small core frame (Position A). Furthermore, the computed data exhibits values that are below those obtained experimentally. This inconsistency can be attributed to the influence of the manufacturing process of the PCC, leading to an irregular dissipation of gaps in the upper yoke. As a result, the existence of these irregular gaps intensifies the quivering displacement of the core. Nevertheless, the computation model fails to consider the influence of the gaps in the upper yoke.

Figure 9(a) displays the deformation of the simulation result. It is shown that the large displacement is at 2 ms for both locations A and location B with their respective value of 5.27×10^{-6} m, 7.02×10^{-6} m. After 10 ms, the cycle restarts.

Figure 9(b) presents the vibration displacement amplitude of the testing result. It is observed that the maximum vibration is at 3 ms and 2 ms for measurement locations A and B with their values of 0.82 V and 0.96 V correspondingly.

Figures 9(a) and 10(a) are graphic illustrations of the cores simulation result in Transient Structural Analysis on a time period of 10 ms for the PCC and CTDCC, respectively.

The comparison between computation values and testing values of the vibratory displacement at location 2 (the top surface central location) and location 9 (the core column measurement position) of the CTDCC is illustrated in Fig. 10.

It is evident that the computed vibration displacement wave shape closely matches the testing with tiny divergences. The reason behind this phenomenon lies in the typical configuration of the CTDCC assembly, which involves tightly compressed sheets of strip materials, consequently reducing the number of internal gaps within the core. Hence, the Maxwell electromagnetic force present within the air gap is negligible, and the main factor of core vibration attributed to the magnetostrictive force resulting from the magnetostrictive effect of the amorphous alloy material.

The testing results indicate that the computed vibration amplitudes are the smallest on the core column at location 9. This disparity can be attributed to the fact that the computation does not take into account the contact between the coil and the core. Conversely, throughout the experiment, the core column was encircled by coils, potentially impacting the outcomes of the vibration measurements conducted on the core column.

In conjunction with Fig. 9 and Fig. 10, it is evident that CTDCC has the ability to diminish the core surface vibration in comparison to PCC. The upper surface of PCC exhibits a large vibration displacement amplitude at location B, while CTDCC

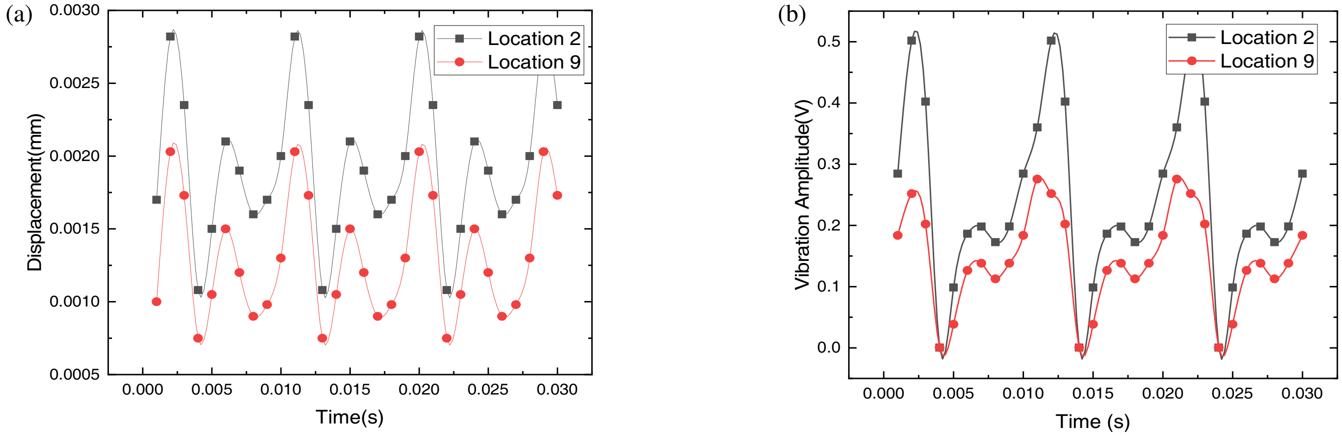

FIGURE 10. Computation and testing comparison of the CTDCC displacement; (a) Simulation, (b) Testing.

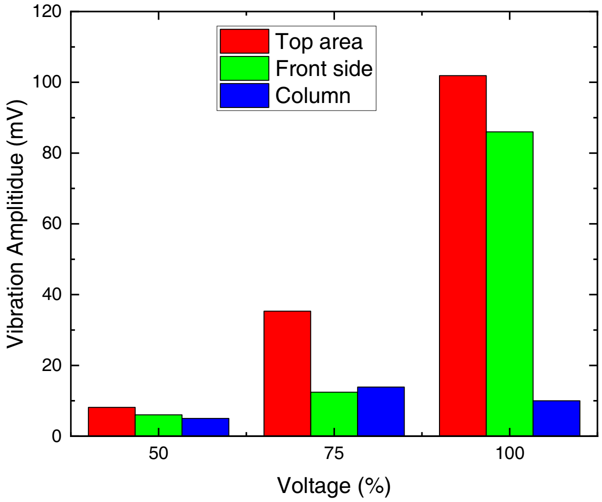

FIGURE 11. Displacement at each section of the CTDCC.

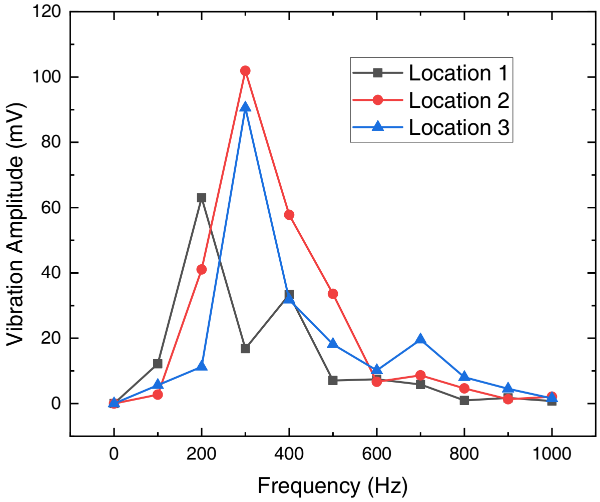

FIGURE 12. Oscillation displacement at each measurement point on the top side of the core.

displays a lower amplitude (location 2). Further analysis is required to examine vibration characteristics of the amorphous alloy CTDCC due to the significant difference in vibration displacement amplitude between the CTDCC and PCC, stemming from their structural variations. As shown in the simulation result, large vibration displacement is on the top surface of the core. It is essential to compare the testing and calculation results of the PCC and CTDCC on the top surface of cores.

1) In calculation, Fig. 9(a) and Fig. 10(a) represent the deformation of the PCC and CTDCC, respectively, in which it is observed that large deformation is on the top core surface (location B and location 2) at 2 ms with their respective values of 7.02×10^{-6} m and 2.82×10^{-6} m. Therefore, CTDCC displayed a lower deformation than PCC.

2) In testing, Fig. 9(b) and Fig. 10(b) denote the vibration amplitude of the PCC and CTDCC correspondingly, wherein it is shown that the maximum vibration amplitude is as well on the upper surface of the core at 2 ms with the values of 0.96 V and 0.5 V correspondingly to the PCC and CTDCC. Thus, the testing result has shown that the vibration amplitude of CTDCC is smaller than that of PCC.

5.2. Vibration Features Analysis of CTDCC

Piezoelectric sensor measures the vibration acceleration data at the measuring location, which is then subjected to double integration to determine the vibration displacement at that specific location. The average vibration displacement magnitude of each location is calculated by averaging the vibration displacement magnitudes of the location under various excitation voltages, as illustrated in Fig. 11. The vibration displacement magnitudes of the measurement locations show a proportional dissipation under varying voltage excitations. An increase in excitation voltage leads to more prominent vibrations on the top area of the cores.

Based on the observations made from Fig. 11, the following points can be deduced:

1) The high vibration magnitude is observed on the upper core surface, while the lower one is found on the core column. At the saturated voltage, the magnitudes on the upper surface and core column measure around 102 mV and 10 mV, correspondingly.

2) The top side of the cores is slenderer than other areas of the cores, with the vibration measurement point running par-

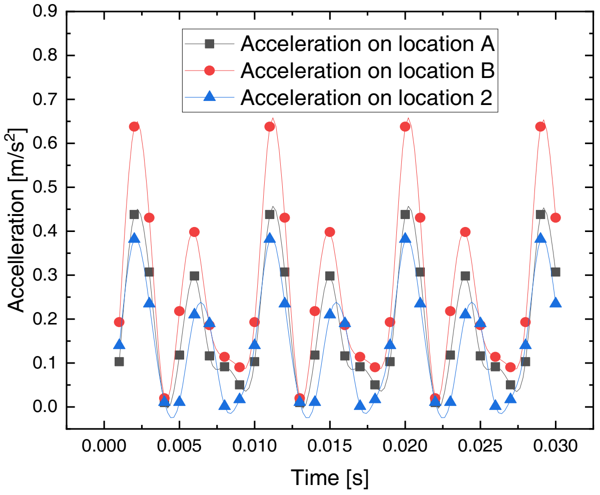

FIGURE 13. Acceleration comparison range between the PCC on locations A, B and CTDCC at location 2.

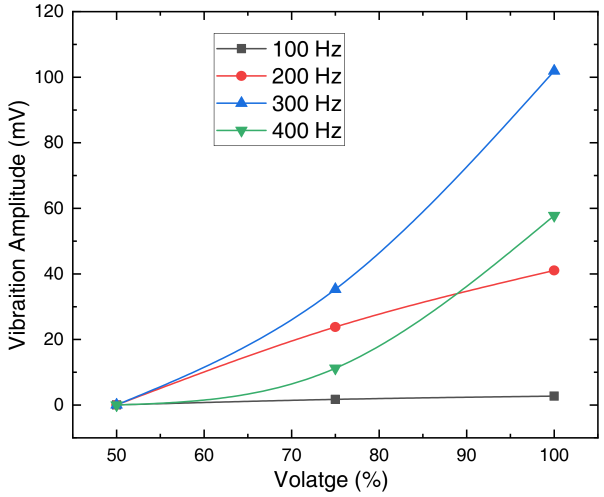

FIGURE 14. Relationship between the vibration and voltage on location 2.

allel to the surface of the wound amorphous strip. Vertically, the vibrations demonstrate a superposition phenomenon, leading to the highest vibration magnitude on the upper yoke of the amorphous core.

Locations 2, 5, and 9 represent the maximum vibration point corresponding to the top area, front side, and column.

5.2.1. Top Side Core Vibration Analysis

The oscillation outcomes of the three measurement locations on the top side are illustrated in Fig. 12. The vibration displacement magnitudes of the measurement locations show a disproportional dissipation under varying frequencies. The maximum vibration amplitude is observed at location 2 at 300 Hz. When being subjected to the saturated voltage, the vibration dislocation magnitudes at locations 2 and 3 can attain 102 mV and 91 mV at 300 Hz, respectively, while the displacement at location 1 is the largest at 200 Hz with a value of 63 mV. Above the frequency of 300 Hz, the vibration displacement amplitude decreases with the increase of the frequency. Beyond 700 Hz, the oscillation amplitude is smaller and can be ignored.

Figure 13 illustrates the acceleration comparison range between the PCC on locations A, B and CTDCC at location 2, showing the impact of varying times when saturated voltage is applied. With an increase in time, there is a corresponding decrease in the proportion of the magnitude component of vibration acceleration. Large acceleration is at 2 ms on location B with an amplitude of 0.638 m/s^2. On location 2 the maximum acceleration is 0.382 m/s^2 at the same time. The vibration accelerations period is 10 ms. It shows that the acceleration on CTDCC is lower than that on PCC structure which leads to the reduction of the vibration amplitude.

For the analysis of measuring location 2, the high vibration magnitude of 200 Hz, 300 Hz, and 400 Hz elements is considered. The relation between these elements and voltage is represented in Fig. 14. Consequently, the following information can be derived:

a) The relationship between vibration amplitude and voltage is directly proportional, excluding the vibration at 100 Hz which shows a linear trend with almost constant amplitude.

b) As the voltage increases, the vibration magnitude components at 200 Hz, 300 Hz, and 400 Hz experience a gradual magnitude in their growth rates. Eventually, these frequencies become dominant ones in terms of vibration. At saturated voltage, the maximum values for these components can reach 41 mV, 102 mV, and 58 mV, correspondingly. Hence, when executing measures to reduce vibration at the dominant location 2, it is crucial to take into account frequencies 300 Hz and 400 Hz, which have the most vibration at the saturated voltage.

5.2.2. Front Side Core Vibration Analysis

Three different percentages of excitation voltages, 50%, 75%, and 100% were applied to the system, resulting in different vibration displacement magnitudes at measurement locations 4 to 6 on the front side surface as illustrated in Fig. 15. It is evident that when the excitation voltage is at 50%, the variations in vibration magnitudes at measurement locations on the front side of the core are negligible. At location 5, it is observed that the most vibration displacement is at the saturated voltage with an amplitude of 89 mV.

Figure 16 illustrates the acceleration spectrum at the dominant measurement location 5, which is situated on the front side of the core. The graph displays the spectrum for different times on a period of 10 ms. The acceleration magnitudes on the front side exhibit a slight decrease compared to those on the top surface of the core (see Fig. 13, acceleration on location 2) when being subjected to identical excitation voltage. The large vibration acceleration at location 5 is 0.306 m/s^2 at 2 ms, while it is 0.382 m/s^2 at location 2 for the same time.

For the analysis of measurement location 5, the vibration displacement magnitudes at the frequencies of 400 Hz, 500 Hz, and 700 Hz are considered, and their correlation with voltage is illustrated in Fig. 17. The following information can be derived:

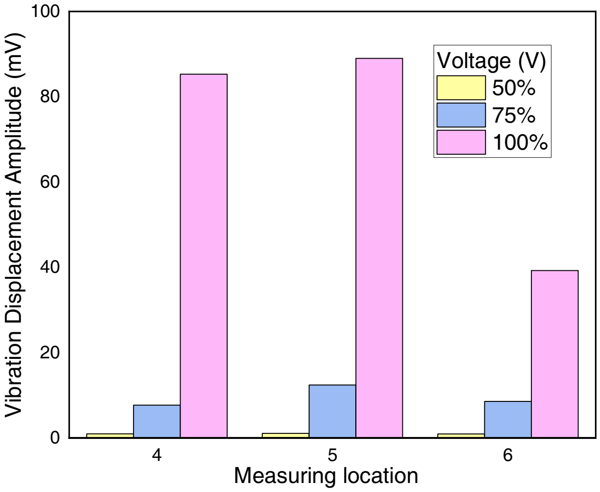

FIGURE 15. Displacement magnitude at each measurement point on the front side of the core.

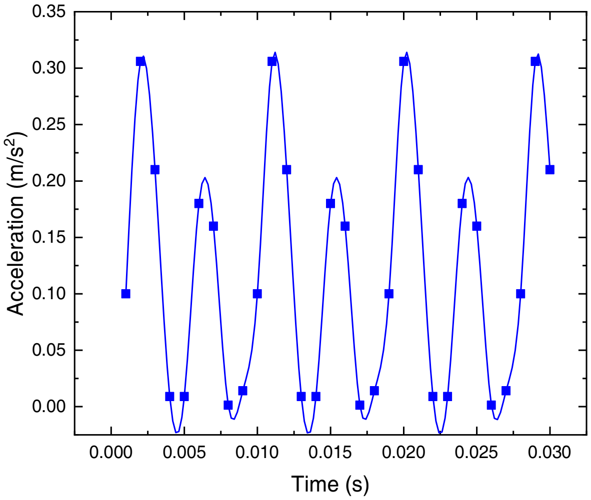

FIGURE 16. Acceleration range at location 5.

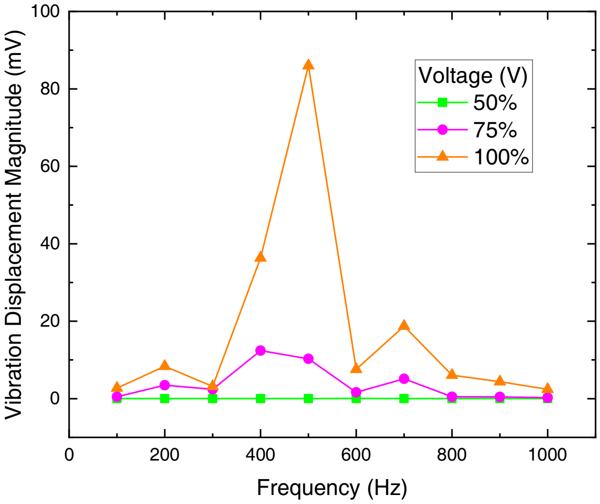

FIGURE 17. Vibration displacement range at location 5.

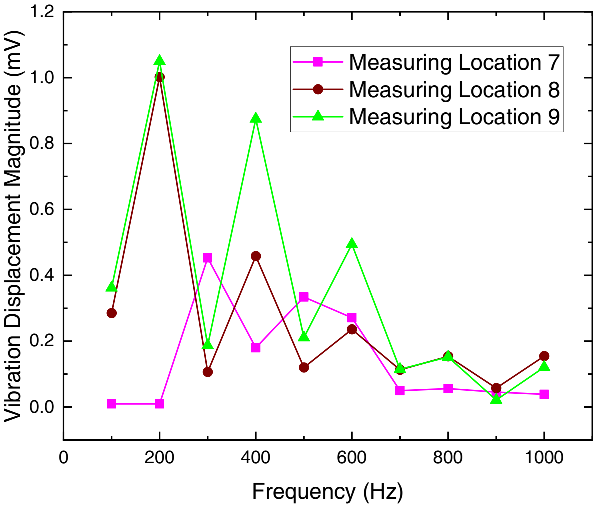

FIGURE 18. Displacement at each measurement point on the core column.

a) The increase in excitation voltage leads to an elevation in all spectral components. Specifically, the rate of the increase for 500 Hz progressively intensifies, suggesting that as the voltage reaches saturation, the presence of higher-frequency vibration displacement range becomes more obvious.

b) The variations in the magnitude of the vibration amplitude on the front side at 100, 300, 800, 900, and 1000 Hz are comparatively insignificant when the saturated voltage is applied.

5.2.3. Core Column Vibration Analysis

Figure 18 illustrates the vibration displacement at various measurement points along the core column when the voltage attains its saturation. Location 9 situated on the periphery of core column displays greater vibration displacement oscillations than location 8 positioned at the center of the core column. This distinction becomes more evident within the frequency of 300 Hz∼700 Hz. Moreover, once the magnetic induction intensity within the core column attains saturation, the magnitude of vibration displacement at location 7, situated at the internal face of the core column, experiences a notable increase. Large vibration displacement is prominent at 200 Hz at location 9 with an amplitude of 1.05 mV. Additionally, the proportion of the 100 Hz component is comparatively lower at location 7. The trend of the vibration amplitude is sawtooth which decreases with an increase of the frequency.

A prominent distinction in vibration acceleration exists between inward and outward sections of the core column, leading to distinct vibration properties. Fig. 19 illustrates the difference in vibration acceleration spectrum in function of time at location 9 on the outside of the core column. The vibration acceleration at location 9 exhibits a large vibration acceleration at 2 ms with a value of 0.22 m/s^2.

Figure 20 illustrates the correlation between vibration displacement and voltage at the measurement location 9, taking into account components of the vibration spectrum from 100 Hz∼600 Hz. The following relationship can be derived from the data.

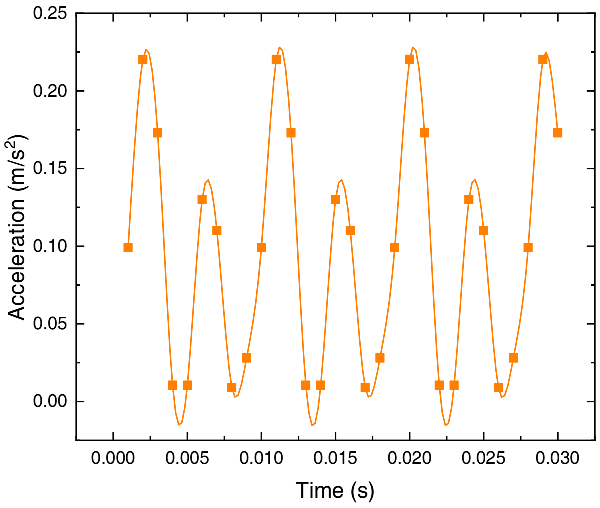

FIGURE 19. Acceleration range at location 9.

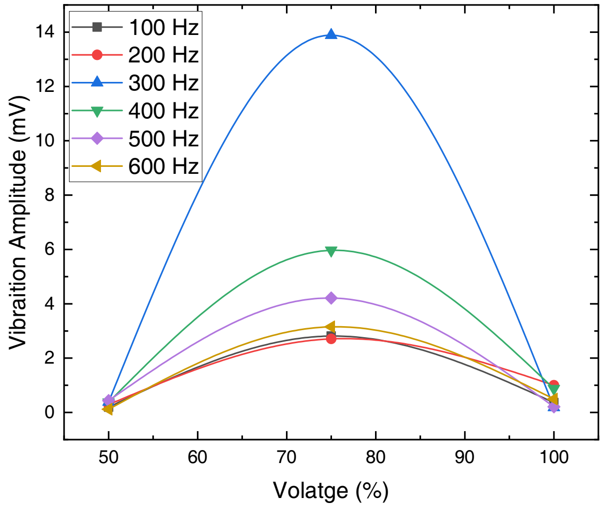

FIGURE 20. Vibration range at location 9.

a) At location 9, despite the gradual increase in growing rates of the vibration amplitude at 75% of the voltage, the main vibration frequency remains at 100 Hz. The more visible vibration magnitudes are at the frequencies of 300 Hz, 400 Hz, and 500 Hz with their respective values of 13.8 mV, 6 mV, and 4.2 mV.

b) Beyond the excitation voltage of 75%, the vibration magnitude decreases proportionally with the increase of the excitation voltage. The highest amplitude is at 300 Hz.

6. CONCLUSION

This research introduces an innovative finite element analysis model for an amorphous transformer with CTDCC, utilizing principles of magnetic-mechanical coupling. Following this, a test setup is built in order to capture the vibration shift dissipation on the surface of the cores. The principal findings can be summarized in the following manner:

1) CTDCC demonstrates a progressive diminution in surface vibration displacement as one moves from the top section to minor section, with the highest average magnitude of vibration detected on the top core surface. The results of the experiment demonstrate that the vibration displacement magnitudes on top surfaces of the CTDCC and PCC are 0.5 V and 0.96 V, respectively, when being subjected to the rated voltage. To a certain degree, the implementation of a CTDCC assemblage has the potential to mitigate surface vibrations.

2) As the excitation voltage rises, the percentage of high-frequency elements in the vibration displacement at each section also rises accordingly. The primary oscillation frequency of the top surface of the CTDCC is 100 Hz. The vibration acceleration magnitude on the column of the core is marginally low compared to the top surface. Additionally, there are slight variations in the magnitudes at each measurement location. As we move towards the outer side of the core column (location 9), magnitudes of the vibration displacement progressively intensify. The primary vibration frequency at the external of the core column is 100 Hz, whereas the interior is predominantly influenced by magnetostrictive nonlinear properties of the material, exhibiting a main vibration frequency of 200 Hz.

3) This solution is particularly suitable for installation environments that necessitate minimal operational noise levels. It is also well-suited for locations housing sensitive instruments or equipment, such as data centers, where low harmonic distortion is essential, or for applications requiring an isolating transformer.

This investigation provides essential insights for engineering applications in areas of mining transformers, traction transformers, marine transformers, and specialized transformers, especially those required to meet strict non-combustibility regulations in building construction.

4) To improve the accuracy of vibration displacement simulations, it is beneficial to analyze the key building factors that pertain to triangular wound core structures in the future.

ACKNOWLEDGEMENT

This research framework is supported by the National Natural Science Foundation of China (52167017), Jiangxi Natural Science Foundation (20224BAB204054), and Ganpo Elite Talent Support Program-Leading Figures in Academic and Technical Fields-Leading Figures (Academic) (20232BCJ22006).

REFERENCES

[1] Gao, J. E., H. X. Li, Z. B. Jiao, Y. Wu, Y. H. Chen, T. Yu, and Z. P. Lu, "Effects of nanocrystal formation on the soft magnetic properties of fe-based bulk metallic glasses," *Applied Physics Letters*, Vol. 99, No. 5, 052504, 2011.

[2] Zhang, J., R. Cui, Y. Wei, D. Yu, S. Xie, S. Fang, and J. Shen, "Optimization and experimental validation of amorphous alloy high-speed asynchronous motor for simultaneous reduction on core and copper losses," *IEEE Access*, Vol. 11, 101112–101122, 2023.

[3] Li, Y., Z. Yang, C. Zhang, and S. Mu, "Vibration and noise measurement of medium-high frequency transformer cores under non-sinusoidal excitation," *IEEE Transactions on Magnetics*, Vol. 58, No. 8, 1–5, 2022.

[4] Zhu, L., J. Hao, and L. Lu, "Research on influence of damping on the vibration noise of transformer," *IEEE Access*, Vol. 10, 92 128–92 136, 2022.

[5] Zhang, P. and L. Li, "Vibration and noise characteristics of high-frequency amorphous transformer under sinusoidal and non-sinusoidal voltage excitation," *International Journal of Electrical Power & Energy Systems*, Vol. 123, 106298, 2020.

[6] Liu, D., J. Li, R. K. Noubissi, S. Wang, X. Xu, and Q. Liu, "Magnetic properties and vibration characteristics of amorphous alloy strip and its combination," *IET Electric Power Applications*, Vol. 13, No. 10, 1589–1597, 2019.

[7] Du, B. X. and D. S. Liu, "Dynamic behavior of magnetostriction-induced vibration and noise of amorphous alloy cores," *IEEE Transactions on Magnetics*, Vol. 51, No. 4, 1–8, 2015.

[8] Mohammed, O. A., S. Liu, and N. Abed, "Study of the inverse magnetostriction effect on machine deformation," in *IEEE SoutheastCon, 2004. Proceedings.*, 433–436, Greensboro, NC, USA, Mar. 2004.

[9] Fonteyn, K. A., A. Belahcen, P. Rasilo, R. Kouhia, and A. Arkkio, "Contribution of Maxwell stress in air on the deformations of induction machines," *Journal of Electrical Engineering & Technology*, Vol. 7, No. 3, 336–341, May 2012.

[10] Delaere, K., W. Heylen, K. Hameyer, and R. Belmans, "Local magnetostriction forces for finite element analysis," *IEEE Transactions on Magnetics*, Vol. 36, No. 5, 3115–3118, 2000.

[11] Besbes, M., Z. Ren, and A. Razek, "Finite element analysis of magneto-mechanical coupled phenomena in magnetostrictive materials," *IEEE Transactions on Magnetics*, Vol. 32, No. 3, 1058–1061, 1996.

[12] Hilgert, T., L. Vandevelde, and J. Melkebeek, "Comparison of magnetostriction models for use in calculations of vibrations in magnetic cores," *IEEE Transactions on Magnetics*, Vol. 44, No. 6, 874–877, 2008.

[13] Zhang, P., L. Li, Z. Cheng, C. Tian, and Y. Han, "Study on vibration of iron core of transformer and reactor based on maxwell stress and anisotropic magnetostriction," *IEEE Transactions on Magnetics*, Vol. 55, No. 2, 1–5, 2019.

[14] Wu, S., W. Li, W. Tong, and R. Tang, "Electromagnetic vibration and noise comparison of amorphous metal PMSMs and silicon steel PMSMs," *IEEE Access*, Vol. 7, 62 672–62 680, 2019.

[15] Mizuta, T., Y. Tani, and K. Fujiwara, "Magnetic property of amorphous magnetic thin ribbon and its laminated bulk under tensile and compressive stresses," *IEEE Transactions on Magnetics*, Vol. 54, No. 11, 1–5, 2018.

[16] Chang, Y.-H., C.-H. Hsu, H.-L. Chu, and C.-P. Tseng, "Magnetomechanical vibrations of three-phase three-leg transformer with different amorphous-cored structures," *IEEE Transactions on Magnetics*, Vol. 47, No. 10, 2780–2783, 2011.

[17] Elhaminia, P., E. Hajipour, and M. Vakilian, "Magnetic flux density determination in 3D wound core transformer using H-balance equation," in *2019 International Power System Conference (PSC)*, 565–570, Tehran, Iran, Dec. 2019.

[18] Hu, J., B. Zhou, Y. Wang, N. Li, Y. Ni, and Z. Gan, "Analysis of vibration characteristics and noise reduction for 10 kV oil-immersed transformer," *Fluctuation and Noise Letters*, Vol. 22, No. 06, 2350048, 2023.

[19] Yang, B., X. Fan, and e. al., "Modeling and no-load characteristics analysis of 3D wound core transformer considering core nonlinearity," *Transactions of China Electrotechnical Society*, Vol. 37, No. 9, 2263–2274, 2022.

[20] Zhou, X. and L. Zhu, "Magnetostrictive simulation of amorphous alloy based on dynamic Jiles-Atherton model," in *The Proceedings of the 9th Frontier Academic Forum of Electrical Engineering*, 765–774, Apr. 2021.

[21] Liu, D., B. Du, M. Yan, and S. Wang, "Suppressing noise for an HTS amorphous metal core transformer by using microperforated panel absorber," *IEEE Transactions on Applied Superconductivity*, Vol. 26, No. 7, 1–5, 2016.

[22] Zhu, L., J. Li, Q. Yang, J. Zhu, and C.-S. Koh, "An improved magnetostriction model for electrical steel sheet based on Jiles–Atherton model," *IEEE Transactions on Magnetics*, Vol. 56, No. 3, 1–4, 2020.

[23] Liu, M., O. Hubert, X. Mininger, F. Bouillault, L. Bernard, and T. Waeckerlé, "Reduction of power transformer core noise generation due to magnetostriction-induced deformations using fully coupled finite-element modeling optimization procedures," *IEEE Transactions on Magnetics*, Vol. 53, No. 8, 1–11, 2017.